Energy Conversion and Management xxx (2009) xxx–xxx

Contents lists available at ScienceDirect

Energy Conversion and Management

journal homepage: www.elsevier.com/locate/enconman

An improved model of induction motors for diagnosis purposes – Slot skewing effect and air–gap eccentricity faults

A. Ghoggal [a,*], S.E. Zouzou [a], H. Razik [b], M. Sahraoui [a], A. Khezzar [c]

[a] Laboratoire de génie électrique de Biskra, Département d'électrotechnique, Université Mohamed Khider, BP 145, Biskra, Algeria
[b] Groupe de Recherche en Electrotechnique et Electronique de Nancy, Université Henri Poincaré, Faculté des Sciences et Techniques, BP 239, F-54506 Vandoeuvre-les-Nancy, France
[c] Laboratoire d'Electrotechnique de Constantine, Université Mentouri, Constantine, Algeria

ARTICLE INFO

Article history:
Received 7 August 2007
Received in revised form 5 June 2008
Accepted 2 January 2009
Available online xxxx

Keywords:
Induction motor
MWFA
Space harmonics
Skew
Axial air–gap eccentricity
Diagnostic

ABSTRACT

This paper describes an improved method for the modeling of axial and radial eccentricities in induction motors (IM). The model is based on an extension of the modified winding function approach (MWFA) which allows for all harmonics of the magnetomotive force (MMF) to be taken into account. It is shown that a plane view of IM gets easily the motor inductances and reduces considerably the calculation process. The described technique includes accurately the slot skewing effect and leads to pure analytical expressions of the inductances in case of radial eccentricity. In order to model the static, dynamic or mixed axial eccentricity, three suitable alternatives are explained. Unlike the previous proposals, the discussed alternatives take into account all the harmonics of the inverse of air–gap function without any development in Fourier series. Simulation results as well as experimental verifications prove the usefulness and the effectiveness of the proposed model.

1. Introduction

The IM break down is commonly the concern of industrial engineers in all fields. Because the needs of increase reliability, improve operation safety and avoid production losses, it is now important to predict too early upcoming abnormalities. Several features of sensor signals have been identified as useful in faults detection and in online protection of IM [1,2]. These include the magnitude of specific spectral components in the stator currents, axial leakage flux and frame vibration [3,4]. The aim of online condition monitoring systems is to trend such features to monitor a severity of a developing fault. However, detailed knowledge of the behaviors of these features is critical for the design of such systems. This must be confirmed by a lot of tests covering a large range of load and faults severity levels in various work conditions.

There are many works devoted to the detection of fault-related current harmonics, and many others dedicated to the modeling and simulation of IM in order to predict the evolution laws of these indicators [5]. In most of them, the related equations are derived from the winding function approach (WFA) [6,7]. This theory has been extended to the well known MWFA which aimed originally the modeling of radial eccentricity [8]. Furthermore, this approach was found powerful because of its ability to consider, jointly or separately, the opening and skewing of the slots, the magnetic saturation and the flux distortion due to the air–gap permeance effect with a relatively small computational time [9,10].

Thanks to the progress in digital measurement technique and signal processing, the famous motor current signature analysis (MCSA) has been very attractive [11,12]. Its application in IM rotor eccentricity detection took much interest in the last years. For the static and dynamic eccentricity, the rotor is shifted from its normal position at the centre of the stator. In the first, the rotor rotates around its axe of symmetry which is not the case in the second type. The principal related spectral components are derived from the general equation given in [13] and described by

$$f_{RSH+dyn} = \left[\left(\frac{N_b \pm n_d}{p}\right)(1-s) \pm 1\right] \cdot f_s \quad (1)$$

In healthy state and static eccentricity, the called principal slot harmonics (PSH) or rotor slot harmonics (RSH) are obtained for $n_d = 0$.

In case of dynamic eccentricity, $n_d = 1, 2, \ldots$ If both types coexist, in the low range frequency appear the harmonics of the mixed eccentricity predicted in [14] and expressed as follows

$$f_{mix} = |f_s \pm k \cdot f_r|, \quad (2)$$

with $k = 1, 2, 3,\ldots$

In practice, the air–gap eccentricity may be caused by many different factors; Unbalanced load, bearing wear, bent rotor shaft and

* Corresponding author.
E-mail address: ghoetudes@yahoo.fr (A. Ghoggal).

0196-8904/$ - see front matter © 2009 Elsevier Ltd. All rights reserved.
doi:10.1016/j.enconman.2009.01.003

Nomenclature

g_0	average air–gap length
g	air–gap function
P	inverse of air–gap function
r	average radius of the air–gap (a polar radius)
r_0	average radius of the air–gap in symmetrical condition
r_j	the jth rotor loop
A,B,C	windings of stator phases A_s, B_s and C_s respectively
$L_{W2.W1}$	mutual inductance between any winding W_1 and W_2 of the motor
l	rotor length
w	number of turns per coil
N_b	number of rotor bars
N_e	number of stator slots
L_b	rotor bar leakage inductance
L_e	end-ring leakage inductance
R_s	stator phase resistance
R_b	rotor bar resistance
R_e	end-ring resistance
J_r	moment of inertia
γ	mechanical angle of the skew
λ_s	pitch of the stator slots
λ_r	pitch of the rotor slots
α	opening of the coil (coil pitch)
β	stator slot width
θ_r	rotor angular position
N	modified winding function
n	distribution function (turns function)
F	the magnetomotive force
f_s	the main frequency (Fundamental frequency)
f_r	rotational frequency
s	slip in per unit
p	number of fundamental pole pairs
n_d	index of dynamic eccentricity
μ_0	permeability in vacuum
δ_s	static eccentricity level
δ_d	dynamic eccentricity level
δ	global eccentricity level
δ_{s0}	static eccentricity level backside of the rotor ($z = 0$)
δ_{d0}	dynamic eccentricity level backside of the rotor ($z = 0$)
L_{st}, L_{dy}	position of the concentric cross section of the rotor in static and dynamic axial eccentricity respectively
C_e	electromagnetic torque
C_r	Load torque
fv	Viscous friction
ω_r	Mechanical speed of the rotor

mechanical resonance at critical load [15]. It is the reason that leads to unbalanced magnetic forces that act both on the rotor and stator of the motor. When the air–gap is not equal along the rotor length of the motor for the same angular position, it is called the axial eccentricity. In this case, the radial force may differ at the low ends of the rotor. Bearing damages, excessive vibration and acoustic noise could be traced to these forces.

In this paper, a model based on an extended form of the MWFA will be developed. One can find that several proposals designed for the modeling of radial air–gap eccentricity. However, few of them specifically allowed the axial non-uniformities. This proposed method is able to include accurately the rotor bar (rotor slot) skewing effect and the radial and axial air–gap eccentricity. Moreover, it leads to pure analytical expressions of the inductances in case of radial eccentricity. Consequently, the computational time is largely decreased thanks to an exact and compact definition of the distribution functions, in contrast to methods based on only an approximation with Fourier series [15]. For all forms of axial eccentricity, three suitable techniques for inductance evaluation are presented.

2. Background

Quite a few diagnosis studies have adopted the MWFA in order to model the radial eccentricity. In these papers, static, dynamic and mixed eccentricities are considered starting from the modeling of the inverse of air–gap function by an approximated expression. In [7,14,15], one can find a model of IM eccentricity based on the use of one harmonic of the inverse of air–gap function, while in [16], the authors prove that the first p harmonics are needed for better results. As for the skewing of the rotor bars, this was modeled in [14,15] thanks to the well known skew factor, whereas the authors of [17] use the description of the inductance per unit of length. This supposes that in any radial section of the motor, the mutual inductance per unit of length is constant.

Following the literature, few attentions in axial eccentricity can be found. For exposing the fact that the air–gap varies according to the axial length of the motor, many designations can be found; shaft misalignment, inclined eccentricity, axial eccentricity or axial nonuniformity. Electromagnetic forces acting between the stator and the rotor when the rotor is misaligned was studied by considering the eccentric motion of the rigid rotor [18]. The treated air–gap eccentricity is expressed as consequences of cylindrical whirling motion, symmetrical conical whirling motion, and combination of both types. Using the magnetic equivalent circuit method, transient and steady state studies of unbalanced magnetic forces in case of rotor misalignment confirm that good evaluation of these forces requires a precise modeling of the inverse of air–gap function [19].

In Ref. [20], the authors verify, from theoretical and practical study of the vibration behaviors, the possibility of detecting some case of shaft misalignment in large induction motors via MCSA. This can be obtained by inspecting the amplitudes of the harmonics given by (2) with $k = \pm 1, +2$ when the level of misalignment increases. The work point out that the rotor vibration in large induction motors will mainly consist of its radial rigid translation or rotation. The modes of vibration were strongly dependent on the bearing stiffness. Once again, and from a viewpoint of air–gap distribution, it was confirmed that these modes can be approximately considered as a combination of dynamic and static axial eccentricity. Thus, a fine modeling of the inverse of air–gap function is quite indispensable.

A first attempt to extend the MWFA to consider the axial nonuniformity for skew and air–gap eccentricity modeling was well performed in [21,22]. It is interpreted as 2D extension of the MWFA. Later on, the rotor saliencies produced by the radial and axial air–gap eccentricity was employed in order to detect the fault from the zero sequence voltage. This was achieved by applying an additional excitation for a short time while the fundamental one is canceled [23]. This approach was aptly exploited because of its ability to include such saliencies in the model. Note that the inductance profiles and the transient behaviors of the operational mode are not yet elucidated. In [15], an exhaustive study of the static axial eccentricity was performed. It was proved that static axial eccentricity demonstrates similar characteristics such as static radial eccentricity. Thus, it can be recognized from the current spectrum, excepting the symmetric case

Please cite this article in press as: Ghoggal A et al. An improved model of induction motors for diagnosis purposes – Slot skewing ... Energy Convers Manage (2009), doi:10.1016/j.enconman.2009.01.003

to the midpoint of the motor shaft. Knowing that only RSHs associated to a non-triplen pole pair can be seen ideally with a balanced power supply and in symmetrical conditions [24], the eccentricity faults are monitored using these frequencies instead of triplen components. Moreover, it was reported that triplen harmonics emerge only due to the constructional and supply unbalances or in case of star stator winding coupling with grounded neutral [22]. To the best knowledge of the readers, none of the denoted works describe the case of dynamic and mixed axial eccentricity, the inductance plots and the associated transient behaviors of the motor. On the other hand, in the analysis of IM having large number of poles, a precise geometrical model must be used, or extra terms of the expansion of the inverse of air–gap function given in [14] must be considered. These are the main goal of this paper.

3. Transient model of the IM

The multiple coupled circuit model supposes that the squirrel cage can be viewed as identical and equally spaced rotor loops [6]. Thus, the current in each mesh of the rotor cage is an independent variable. Using the following assumptions:

- the permeance of the iron is infinite,
- the eddy current, corps saturation and winding losses are negligible,
- there are no inter-bar currents,

one can establish voltage and mechanical equations of the loaded IM for a three-phase stator winding YN-connected (grounded neutral):

$$\begin{cases} [U] = [R][I] + \frac{d([L].[I])}{dt} \\ C_e = [I]^T \cdot \frac{\partial [L]}{\partial \theta_r} \cdot [I] \text{ and } C_e - C_r = J_r \frac{d\omega_r}{dt} \end{cases} \quad (3)$$

$[U]$ corresponds to the system voltages, $[I]$ to the stator and rotor currents. They are $(N_b + 4) \times 1$ matrix. The resistances matrix $[R]$ and the inductances matrix $[L]$ are $(N_b + 4) \times (N_b + 4)$ matrices. In Y-connection (floating neutral), the system must be rearranged as assuring the condition of a null sum of the line currents [28].

4. Inductances calculation

4.1. Types of eccentricities

Fig. 1 is a schematic representation of the static, dynamic and mixed radial eccentricity. To simplify the scheme, only the frame axes are illustrated. The thick line corresponds to the stator natural axis, the thin to the rotor natural axis while the dash-dot line depicts the rotor rotational axis. A concentric rotor means that the denoted axes are superimposed. The pure radial eccentricity is well documented previously. In reality, the most probably case is that the nonuniformity depends from the rotor axial length. An important step in the modeling of axial eccentricity is to imagine how this one can happen. The schematic illustration of Fig. 2 may elucidate this kind of rotor faults.

In static axial eccentricity, the rotor rotates around its natural axis which is inclined compared to the stator one. In dynamic axial eccentricity, the rotor natural axis is inclined compared to its rotational axis, which is superimposed to the stator axis. One can imagine combinations of these modes and those of pure radial eccentricity which are the cases likely to be found in reality. These combined modes represent variants of mixed axial eccentricity.

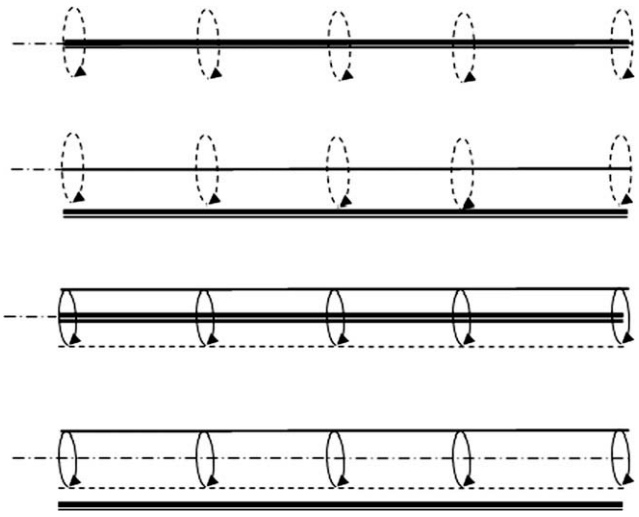

Fig. 1. Illustration of the radial eccentricity. From top to bottom, symmetric case, static, dynamic and mixed radial eccentricity.

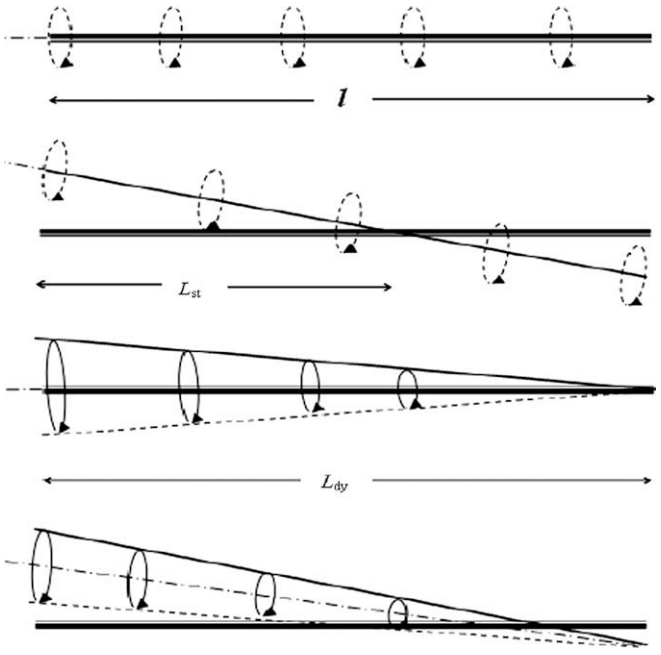

Fig. 2. Illustration of the axial eccentricity. From top to bottom, symmetric case, static (case where $L_{st} < l$), dynamic (case where $L_{dy} = l$) and a variant of mixed axial eccentricity.

4.2. Global formulation

Fig. 3 shows an elementary induction machine model. It consists of two cylindrical masses separated by an air–gap, one for the stator, and one for the rotor. Starting from an arbitrary closed path *abcda,* an extension of the MWFA which considers the axial dimension derives [21,22]. Points *a* and *d* are located on the stator inner surface, while *b* and *c* are located on the external rotor surface. Thus, the distribution function *n* and the inverse of air–gap function g^{-1} corresponding to rotor position θ_r are defined at any of coordinates (φ, z) in space. However, the average value of the inverse of air–gap function $\langle g^{-1} \rangle$ depends only from θ_r measured from the same reference point as for the stator angle φ. The 2D modified winding function (MWF) can be expressed as in (4)

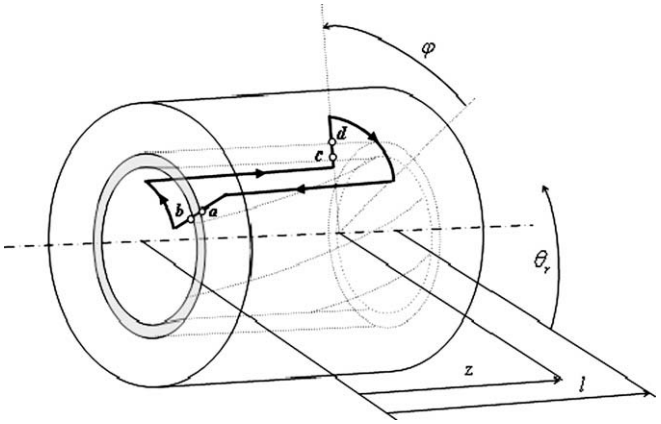

Fig. 3. Elementary induction motor.

$$N(\varphi,z,\theta_r) = n(\varphi,z,\theta_r) - \frac{1}{2\pi l\langle g^{-1}\rangle}\int_0^{2\pi}\int_0^{l} n(\varphi,z,\theta_r) \cdot g^{-1}(\varphi,z,\theta_r)dzd\varphi \quad (4)$$

with

$$\langle g^{-1}\rangle = \frac{1}{2\pi}\int_0^{2\pi}\frac{1}{l}\cdot\left(\int_0^{l} g^{-1}(\varphi,z,\theta_r)\cdot dz\right)\cdot d\varphi \quad (5)$$

The elementary flux in the air–gap measured with respect to an elementary section $ds = dz \cdot d\eta$ is

$$d\phi = \mu_0 F(\varphi,z,\theta_r)\cdot g^{-1}(\varphi,z,\theta_r)\cdot dz\cdot d\eta \quad (6)$$

F is the MMF distribution in the air–gap. In case of eccentricity, the elementary arc $d\eta$ of the limit of ds is not circular (Fig. 4). If we want to take highly into account the non-circular section of air–gap, we must define it using its curvature radius instead of the polar radius r which holds its definition with respect to a fixed point. By means of only r, the arc η can be mathematically approximated by

$$d\eta = \sqrt{(dr/d\varphi)^2 + r^2}\cdot d\varphi \quad (7)$$

In case of eccentricity, the air–gap function is given by [14]

$$g(\varphi,z,\theta_r) = g_0\cdot[1 - \delta_s(z).\cos(\varphi) - \delta_d(z).\cos(\varphi-\theta_r)] \quad (8)$$

Another expression derives

$$g(\varphi,z,\theta_r) = g_0[1 - \delta(z)\cdot\cos(\varphi-\rho(\theta_r))] \quad (9)$$

δ and ρ are function of δ_s, δ_d and θ_r as explained in [14].

The use of (9), leads to the expression giving the average air–gap radius

$$r(\varphi,z,\theta_r) = r_0 + \frac{\Delta g(\varphi,z,\theta_r)}{2}. \quad (10)$$

Then

$$r(\varphi,z,\theta_r) = r_0 - 0.5g_0\cdot\delta(z)\cdot\cos(\varphi-\rho(\theta_r)), \quad (11)$$

and

$$(dr/d\varphi) = 0.5\cdot g_0\cdot\delta(z)\cdot\sin(\varphi-\rho(\theta_r)). \quad (12)$$

The IM have a relatively small air–gap. Since $\delta < 1$, it is easy to notice that

$$\begin{cases} 0.5g_0\cdot\delta(z)\cdot\cos(\varphi-\rho(\theta_r)) < 0.5g_0 \ll r_0 \\ (dr/d\varphi)^2 < 0.25\cdot g_0^2 \ll r^2(\varphi,z,\theta_r) \end{cases}. \quad (13)$$

For physically reasonable values of r and g_0, the approximation (13) holds in most cases. Thus, from (11)–(13) one can assume that $r(\varphi,z,\theta_r) = r_0$, then $d\eta = r_0 d\varphi$. This is the first step in order to get a pure analytical resolution of the integrals leading to IM inductances.

Note that, for a given rotor position, any variable defined initially with respect to φ, z and r, depends now only from φ and z. The magnetic field in the air–gap is projected in a cylindrical surface of radius r_0. Taking $x = r_0\cdot\varphi$, $x_r = r_0\cdot\theta_r$ one can now envisage a plane representation where the skew and the crossing of rotor loops under the field of stator coils become easily and more interpretable (Fig. 5). It is clear that x correctly translates the linear displacement along the arc corresponding to the angular opening φ.

Knowing that N is the MMF per unit of current, the expression giving the flux seen by all turns of coil W_{2j} of any winding W_2 due to the current i_{W1i} flowing in coil W_{1i} of winding W_1 is reduced to

$$\phi_{W2j\cdot W1i} = \mu_0\int_0^{2\pi r_0}\int_0^{l} N_{W1i}(x,z,x_r)\cdot n_{W2j}(x,z,x_r)\cdot g^{-1}(x,z,x_r)\cdot i_{W1i}dzdx. \quad (14)$$

Taking into account the axial asymmetry, $N_{W1i}(x,z,x_r)$ and $n_{W2j}(x,z,x_r)$ could be redefined to describe the slot skewing. In this analysis, we consider only the skewing of rotor bars. The calculation of mutual inductance between stator winding A and rotor loops can be achieved by replacing W_{2j} by a rotor loop r_j and considering that W_{1i} is the *ith* coil A_i of stator winding A. Fig. 5 depicts the displacement of r_j under the field produced by A_i. In Fig. 5, the pitch α_{Ai} of coil A_i is defined with respect to its sides located at $x_{1i} = r_0\cdot\varphi_{1i}$ and $x_{2i} = r_0\cdot\varphi_{2i}$. The total flux $\psi_{W1\cdot W2}$ corresponding to all coils of any winding W_1 and W_2 holds its general expression by summing the elementary fluxes and integrating over the whole surface. Knowing that $L_{W2\cdot W1}$ is this flux per unit of current, yields

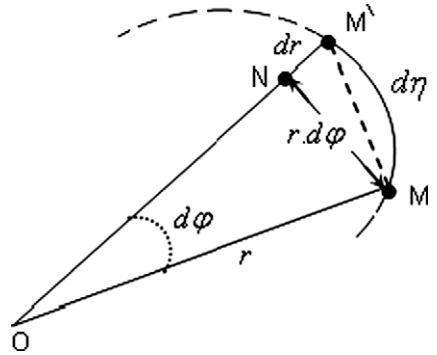

Fig. 4. Representation of the elementary non-circular arc.

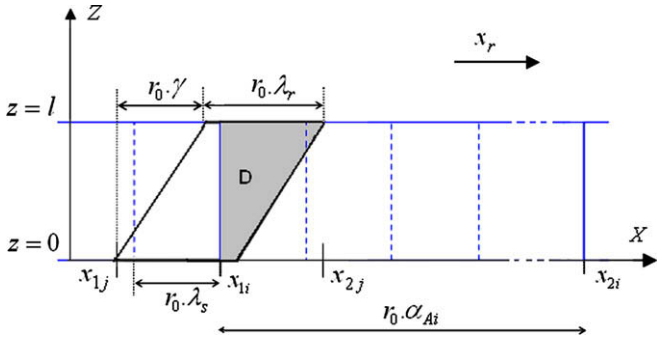

Fig. 5. A plane view of the crossing of rotor bars under the field of stator coils.

$$L_{W2\cdot W1}(x_r) = \mu_0 \int_0^{2\pi r_0} \int_0^{l} N_{W1}(x,z,x_r)\cdot n_{W2}(x,z,x_r) \cdot g^{-1}(x,z,x_r)dzdx. \quad (15)$$

Using (15) and taking $g^{-1}(x,z,x_r) = P(x,z,x_r)$, a new expression can be easily obtained

$$L_{W2\cdot W1}(x_r) = 2\pi r_0 l\mu_0 \left(\left(\sum_{i=1}^{\upsilon} \sum_{j=1}^{\nu} \langle P\cdot n_{W1i}\cdot n_{W2j}\rangle \right) - \frac{\langle P\cdot n_{W1}\rangle \cdot \langle P\cdot n_{W2}\rangle}{\langle P\rangle} \right) \quad (16)$$

where υ and ν are the number of coils of winding W_1 and W_2 respectively. Thus, according to the chosen type of winding, the mutual inductance between W_1 and W_2 depends on the mutual inductances of their elementary coils.

4.3. Radial eccentricity

In general, numerical calculation makes it possible to find the machine inductances. However, an expansion in Fourier series of P can be used to get an analytical solution [16]. Acceptable results are obtained by using the first p harmonics. Then

$$P(x,x_r) = \frac{P_0}{2} + \sum_{i=1}^{p} P_i \cdot \cos[i\cdot(x/r_0 - \rho(x_r))], \quad (17)$$

with

$$P_i = 2\cdot \left(\frac{1}{g_0\sqrt{1-\delta^2}} \right) \cdot \left(\frac{1-\sqrt{1-\delta^2}}{\delta} \right)^i, i = 0,1,\ldots,p \quad (18)$$

As a detailed example, (16) will now be used to calculate the mutual inductance between stator coil A_i and rotor loop r_j. The rotor loop is regarded to be a coil with one turn ($\nu = 1$ in Eq. (16)). Then

$$\langle P\cdot n_{Ai}\cdot n_{rj}\rangle = \frac{1}{2\pi\cdot r_0\cdot l} \int_0^{2\pi r_0} \int_0^{l} n_{Ai}(x).\cdot n_{r_j}(x,z,x_r) \cdot P(x,x_r)dzdx. \quad (19)$$

In [9,14,15] as well as in other papers, a development in Fourier series of the distribution and winding functions is used in order to resolve the integrals analytically. These require a lot of terms in order to approximate the functions. With serve of the proposed plane view, only one term is needed to define these functions exactly. It is clear that such definition decreases considerably the time and calculation process and leads to more accurate results.

According to Fig. 6, for any rotor position x_r the distribution function of rotor loop r_1 can be expressed in 2D as follows:

$$n_{rj}(x,z,x_r) = \begin{cases} 1 & x_{1j}(x_r)\langle x\langle x_{2j}(x_r), z_{1j}(x)\langle z(x)\langle z_{2j}(x). \\ 0 & Otherwise \end{cases} \quad (20)$$

The endpoints of rotor loops depend on x_r because of the rotor relative displacement. In the next steps, we choose simply x_j to indicate $x_j(x_r)$, and we consider only the spatial coordinates x and z in the integral's boundaries. As for z_{1j} and z_{2j}, they are defined as follow

$$z_{1j}(x) = \begin{cases} 0, & x_{1j} \leqslant x \leqslant (x_{1j} + r_0\cdot\lambda_r) \\ \frac{l}{r_0\gamma}(x - x_{1j} - r_0\cdot\lambda_r), & (x_{1j} + r_0\cdot\lambda_r) \leqslant x \leqslant x_{2j} \end{cases} \quad (21)$$

$$z_{2j}(x) = \begin{cases} \frac{l}{r_0\gamma}(x - x_{1j}), & x_{1j} \leqslant x \leqslant (x_{1j} + r_0\cdot\gamma) \\ l, & (x_{1j} + r_0\cdot\gamma) \leqslant x \leqslant x_{2j} \end{cases} \quad (22)$$

where $(x_{2j} - x_{1j}) = r_0(\gamma + \lambda_r)$

By means of (20), (19) becomes

$$\langle P\cdot n_{Ai}\cdot n_{rj}\rangle = \frac{1}{2\pi r_0\cdot l} \int_{x_{1j}}^{x_{2j}} \int_{z_{1j}(x)}^{z_{2j}(x)} n_{Ai}(x)\cdot P(x,x_r)dzdx \quad (23)$$

Following Fig. 7, the expression of the distribution function n_{Ai} for stator coil A_i can be deduced. Note that if the slot width β is taken into account, one can assume that the MMF rise linearly [17].

$$n_{Ai}(x) = \begin{cases} \frac{w_{Ai}}{r\cdot\beta_0}(x - x_{1i}) & x_{1i} \leqslant x \leqslant (x_{1i} + r_0\cdot\beta) \\ w_{Ai} & (x_{1i} + r_0\cdot\beta) \leqslant x \leqslant (x_{1i} + r_0\cdot(\beta + \alpha_{Ai})) \\ \frac{-w_{Ai}}{r\cdot\beta_0}(x - x_{2i}) & (x_{1i} + r_0\cdot(\beta + \alpha_{Ai})) \leqslant x \leqslant x_{2i} \\ 0 & Otherwise \end{cases} \quad (24)$$

According to (24), when the rotor loop is partially under the field of the stator coil, it is obvious that the integral in the external interval is null. Then, the integral of (23) becomes a surface integral over 'D'.

$$\langle P\cdot n_{Ai}\cdot n_{rj}\rangle = \frac{1}{2\pi r_0 l_0} \int\int_D n_{Ai}(x)\cdot P(x,x_r)dzdx \quad (25)$$

where 'D' is the common surface (grey region in Fig. 5) among the surface of projection of rotor loop r_j and that of stator coil A_i. Using the above relationships, the integral of (25) can be analytically resolved. In the particular case of a uniform air–gap and $\beta = 0$, n_{Ai} is constant in 'D'. According to $S_D(x_r)$ which is the area of 'D', Eq. (25) can be written as

$$\langle P\cdot n_{Ai}\cdot n_{rj}\rangle = \frac{w_{Ai}\cdot S_D(x_r)}{2\pi r_0 l\cdot g_0}. \quad (26)$$

Regarding $\langle P\cdot n_A\rangle$ and $\langle P\cdot n_{rj}\rangle$, and due to the fact that they are independent from rotor position x_r, their values are easily deduced from the two expressions:

$$\langle P\cdot n_A\rangle = \frac{\langle n_A\rangle}{g_0} \quad (27)$$

$$\langle P\cdot n_{rj}\rangle = \frac{1}{N_b\cdot g_0} \quad (28)$$

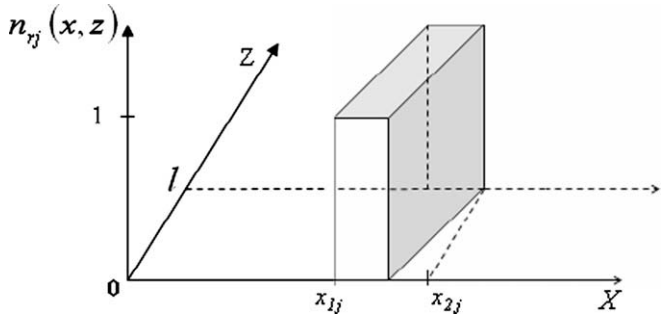

Fig. 6. The 2-D distribution function of rotor loop r_j for a known rotor position.

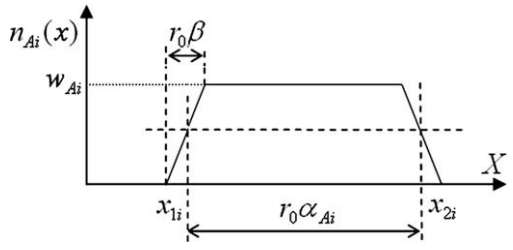

Fig. 7. The turn function of coil A_i.

In general, the calculation of L_{r1A} is similar to the calculation of the volume having the base '*D*', and to the calculation of the area of '*D*' itself in case of constant air–gap and a neglected slot width ($\beta = 0$). Following the same procedures and the position of coils in the slots, their connection and their polarities, it will be possible to find the double sum in (16) and, then, the inductance value. The resulting algorithm is easily adaptable to any winding and no need for look-up table containing the inductance values as in [6].

4.4. Axial eccentricity

Let us revaluate just (25). Referring to Fig. 2, and supposing that the eccentricity levels rise linearly along the rotor shaft for the same angular position, yield [25]

$$\delta_s(z) = \delta_{s0}\left(1 - \frac{z}{L_{st}}\right) \tag{29}$$

$$\delta_d(z) = \delta_{d0}\left(1 - \frac{z}{L_{dy}}\right) \tag{30}$$

Note that, for fixed values of δ_{s0} and δ_{d0}, the choice of L_{st} and L_{dy} identifies the shaft misalignment level. Sometimes, though, the integral will be difficult or we would not even be able to evaluate it, it can be made easier by using suitable numerical integration to convert the integral into a simple some of terms. Based on the described model, we discuss three alternatives to evaluate the integral of (25).

The first solution use one of the classical numerical double integration. If we choose the known midpoint approximation to estimate (25) using (8), for a given position of the rotor, divide the rectangular region of $(x_{2j} - x_{1j}) \cdot l$ into $m_x \cdot m_z$ squares of length h yields

$$F(x_r) = \sum_{i=1}^{m_x}\sum_{j=1}^{m_z} f(x_i, z_i, x_r).H(x_i, z_i, x_r) \cdot h^2 \tag{31}$$

with

$$f(x_i, z_i, x_r) = n_{Ai}(x_i) \cdot P(x_i, z_i, x_r), \tag{32}$$

$$h = \frac{l}{m_z} = \frac{(x_{2j} - x_{1j})}{m_x} \tag{33}$$

and

$$\langle P \cdot n_{Ai} \cdot n_{rj} \rangle \approx \frac{1}{2\pi r_0 \cdot l} F(x_r). \tag{34}$$

H equal unity if (*x*,*z*) is in '*D*' and zero otherwise. It should be noted that this is one of the evident ways to resolve a double integration numerically.

The second proposal is based on a rearrangement of (23) as:

$$\langle P \cdot n_{Ai} \cdot n_{rj} \rangle = \frac{1}{2\pi r_0 \cdot l} \int_{x_{1j}}^{x_{2j}} \left[n_{Ai}(x) \cdot \int_{z_{1j}(x)}^{z_{2j}(x)} P(x, z, x_r) dz \right] .dx \tag{35}$$

Following (8), (29), and (30), *P* can be written like

$$P(x, z, x_r) = \frac{1}{C + z \cdot E} \tag{36}$$

where

$$C = 1 - \delta_{s0} \cdot \cos(x/r_0) - \delta_{d0} \cos((x - x_r)/r_0) \tag{37}$$

$$E = \left(\frac{\delta_{s0}}{L_{st}}\right) \cdot \cos(x/r_0) + \left(\frac{\delta_{d0}}{L_{dy}}\right) \cdot \cos((x - x_r)/r_0) \tag{38}$$

Substituting (36) into (35) yields

$$\langle P \cdot n_{Ai} \cdot n_{rj} \rangle = \frac{1}{2\pi r_0 \cdot l} \int_{x_{1j}}^{x_{2j}} \left[\frac{n_{Ai}(x)}{E} \cdot Log\left(\frac{C + z_{2j}(x).E}{C + z_{1j}(x).E}\right) \right] \cdot dx \tag{39}$$

At this stage, a simple numerical integration instead of double integration could be used to evaluate (39).

The third alternative consists on the use of an appropriate Monte Carlo (MC) integration. Maybe the integral of (25) has an analytical solution, but many multiple integrals are not so easily evaluated in which case MC integration is a useful alternative. MC integration is not usually a computationally viable alternative to other methods of integration such as Simpson's rule. However, it can be of some value in solving double and multiple integrals [26]. A simple MC method for evaluating a two-dimensional integral uses the same rectangular region as in the first alternative, but the *m* points of coordinates (x_i, z_i) are chosen at random within the rectangle. This can be done easily using uniform random numbers for each dimension at a time [27].

The estimate for the integral is then

$$F(x_r) = \frac{\Omega}{m} \sum_{i=1}^{m} f(x_i, z_i, x_r) \cdot H(x_i, z_i, x_r) \cdot h^2, \tag{40}$$

where Ω is the area of the rectangle $l.(x_{2i} - x_{1i})$. In general, (40) represents the area of the region 'D' multiplied by the average value of $f(x, z)$ in '*D*'. Comparison of 31, 39, and 40, illustrates a crucial difference; in classical numerical integration, we need two different sums, but in MC integration as well as in the second proposed alternative, only one is enough. In the literature, one can find that this MC variant is known as a hit and miss method. Note that, unlike the few attempts denoted in Section 2, the proposed alternatives consider all the harmonics of the inverse of air–gap function. This may lead to more accurate signal spectra, especially, in the study of IMs having a large number of poles. Furthermore, the reduction of the double numerical integration (double sum) into one simple integration can lead to a considerable decreasing on the time and calculation process.

5. Simulation results

5.1. Inductances calculation

The studied machine is a three-phase two-pole star connected 3 kW IM. Reader can find in the Appendix the motor parameters. The skew of rotor bars has a largest impact on eccentricity harmonics. For that, it is taken into account in the simulation as well as the linear rise of the MMF across the stator slots. However, the slot effects may not be very important according to the study of [9]. Average core saturation effect can be included as described in [10]. The particularity of the MWFA is that it can evaluate these effects individually and in a relatively short computation time compared to finite element methods. Whilst the above analysis makes a number of simplifying assumptions, it identifies the significant harmonics one would expect to observe in the stator current spectrum of the motor.

Fig. 8 shows the mutual inductances L_{r1A} between stator winding *A* and the first rotor loop r_1. The two cases considered differ by the presence or not of the stator slot opening and rotor bar skewing. The mutual inductance between winding *A* and the second rotor loop is identical to the mutual inductance with the first rotor loop, except that it is shifted by an angle $\lambda_r = 2\pi/N_b$.

As for windings *B* and *C*, L_{r1B} and L_{r1C} are also similar, but shifted by $2\pi/3$. In Fig. 8, the first derivative of the mutual inductance L_{r1A} is also given for the opening and skew conditions. As shown, the rotor bars skewing produces a significant effect on the magnitude of the first derivative of the mutual inductance. Fig. 9 depicts the modification in the curves caused by the air–gap eccentricity. Note that the linear rise of MMF a cross stator slots has a minor effect in the shape of the inductance curves and theirs derivatives compared to the rotor bar skewing [17].

Please cite this article in press as: Ghoggal A et al. An improved model of induction motors for diagnosis purposes – Slot skewing ... Energy Convers Manage (2009), doi:10.1016/j.enconman.2009.01.003

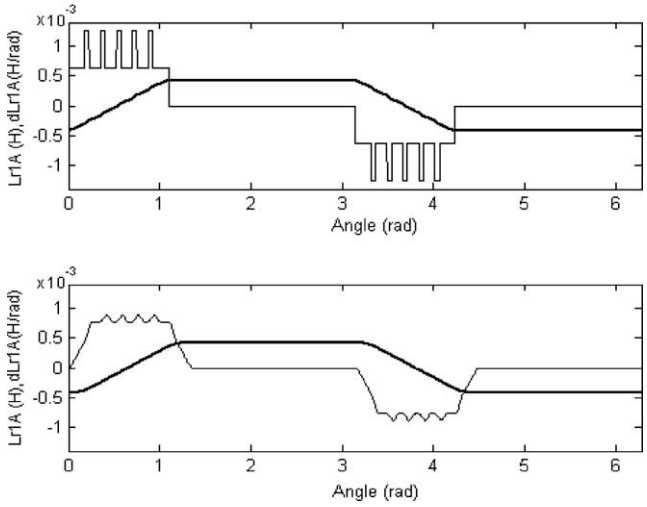

Fig. 8. L_{r1A} (thick line) and its derivative (thin line) in case of symmetric machine. Without skew and slot opening (top), with skew and slot opening (bottom).

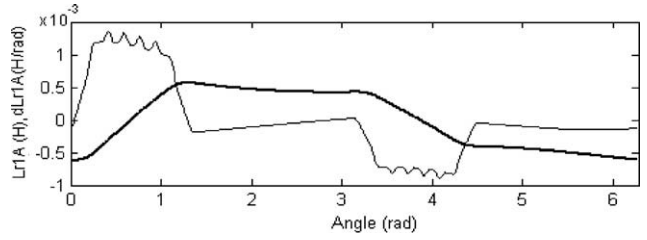

Fig. 9. L_{r1A} and its derivative in case of static radial eccentricity of 20%.

In both static radial and static axial eccentricity, since the air–gap picture doesn't change with rotor movement, the self and mutual inductances of the stator windings will be independent of the rotor position. However, they will change with respect to rotor position in case of dynamic eccentricity (Fig. 10). In case of axial eccentricity, their absolute values increase when the coefficient corresponding to the position of the concentric cross section of the rotor (L_{dy}) increases. A huge value of L_{dy} (like 1 m and more) leads to a pure radial eccentricity (Fig. 11).

As a consequence of static axial eccentricity, the rotor loop self inductance and mutual inductances between rotor loops are function of rotor position. They describe the same characteristics of pure radial eccentricity presented in Fig. 12, but there values depend on the shaft misalignment level. Fig. 13 depicts the curve of the mutual inductance between the first and second rotor loop as a function of L_{st} and the rotor position.

The effect of dynamic axial eccentricity in the variation of mutual inductance L_{r1A} with respect to the rotor angular position

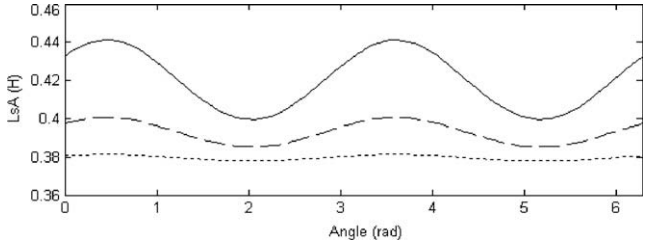

Fig. 10. Self inductance of stator winding A in dynamic radial eccentricity of 20% (dot line), 40% (dash line) and 60% (solid line).

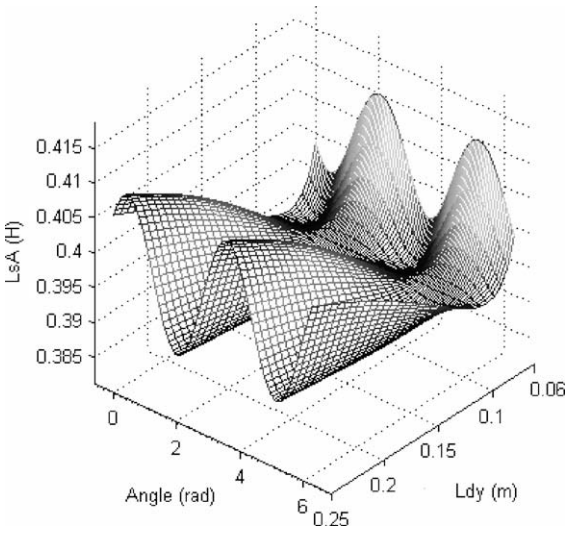

Fig. 11. Self inductance of stator winding A in dynamic axial eccentricity of $\delta_{d0} = 60\%$, and $L_{dy} = 0.5 \times l \ldots 2 \times l$.

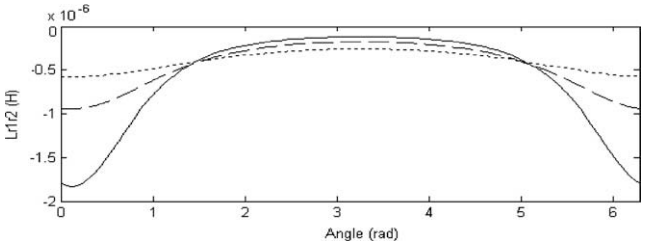

Fig. 12. Mutual inductance between the first and the second rotor loop in static radial eccentricity of 20% (dot line), 40% (dash line) and 60% (solid line).

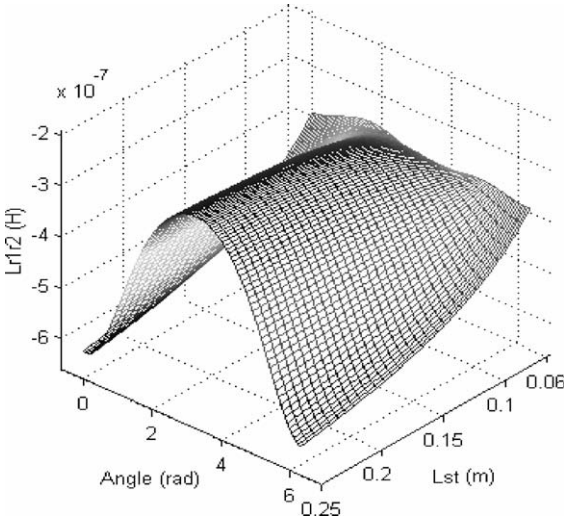

Fig. 13. Rotor mutual inductance between the first and second rotor loop in static axial eccentricity of $\delta_{s0} = 50\%$ and $L_{st} = 0.5 \times l \ldots 2 \times l$.

(from 0 to 2π) and the degree of shaft misalignment (L_{dy} from half l to $2.5 \times l$) is shown in Fig. 14. It can be seen that the inductances for an axial eccentricity case describe the same characteristic of radial eccentricity whose level is the average value of the eccentricity levels at the two ends of the machine in the actually axial eccentricity. Thus theoretically, the fault- related harmonics would become undetectable for the case with average zero dynamic

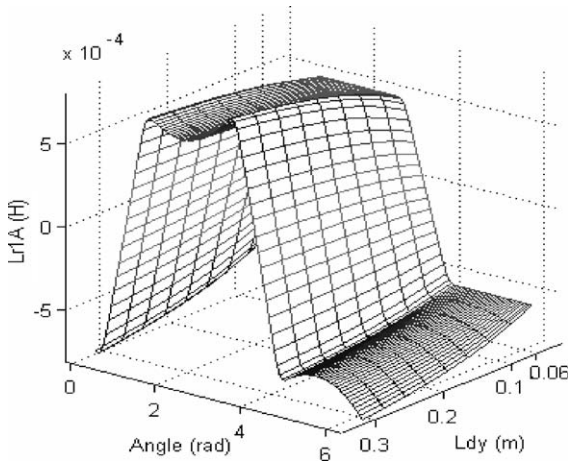

Fig. 14. Mutual inductance between stator winding A and rotor loop r_1 in dynamic axial eccentricity of $\delta_{d0} = 70\%$ for different values of L_{dy}.

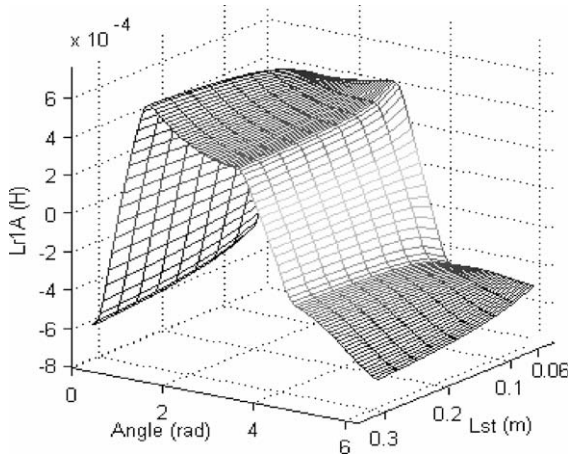

Fig. 15. Mutual inductance between stator winding A and rotor loop r_1 in static axial eccentricity of $\delta_{s0} = 50\%$ for different values of L_{st}.

eccentricity ($L_{dy} = l/2$). The same analysis as for the static axial eccentricity and Fig. 15.

5.2. Dynamic simulation

The next simulation results predict the torque and speed wave form in addition to the current spectra when the motor is fed from a sine wave symmetrical voltage supply. Based on the IM model described above, a numerical simulation of the transient startup is performed. The frequency spectra of line current are obtained thanks to the Fast Fourier Transform (FFT) using a Hanning's window. It is drawn in the logarithmic magnitude scale and normalized format. The magnitude of the fundamental is assigned to the value of 0 dB. In all the simulation, 75% of the full load (10 N m) is applied.

5.2.1. Healthy state

Figs. 16 and 17 show the transient dynamic start up behaviors of the IM under no load condition. At $t = 0.6$ s load is applied. As can be seen, the use of skewing reduces the average value and the oscillations of the speed as well as the parasitic torque at steady state. It is, of course, to eliminate such effects that skew is employed in the real machines. Fig. 18 shows the stator current at steady state for a loaded machine. Once again, if skew is neglected a slot ripples rise in the computed results [29].

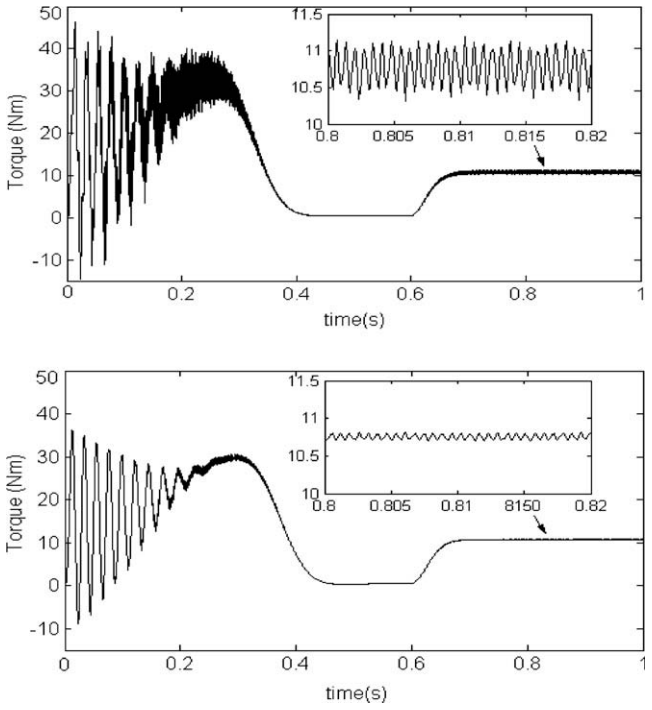

Fig. 16. Electromagnetic torque. Without skew (top), With skew (bottom). Motor in healthy state.

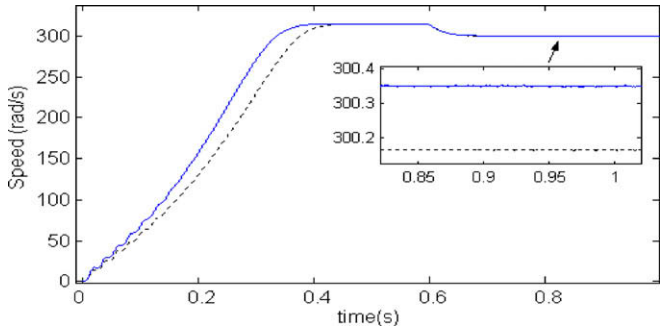

Fig. 17. Rotational speed. Without skew (solid line) and with skew (dot line). Motor in healthy state.

5.2.2. Radial eccentricity

Fig. 19 represents the line current spectra of the studied IM operating in mixed radial eccentricity condition. The stator winding is YN-connected. In the low range frequency, it is possible to see the mixed eccentricity components of Eq. (2).

It is now clear that the presence of RSHs in line current of three-phase IM is primarily dependent on the number of rotor slots and number of fundamental pole pairs of the machine. It was also shown in previous works that only RSHs associated to a non-triplen pole pair can be seen ideally with a balanced power supply and in symmetrical conditions [24] (the pole pair number is obtain when dividing (1) by f_s and making $s = 0$). Owing to the fact that the voltage sum contains extraneous frequencies due to the slot harmonics and/or inverter drives switching and load dependence core saturation, the neutral potential of the motor is non-null even under balanced voltages. Then, the condition of a null sum of the line currents is not verified if the neutral point is grounded. This is the

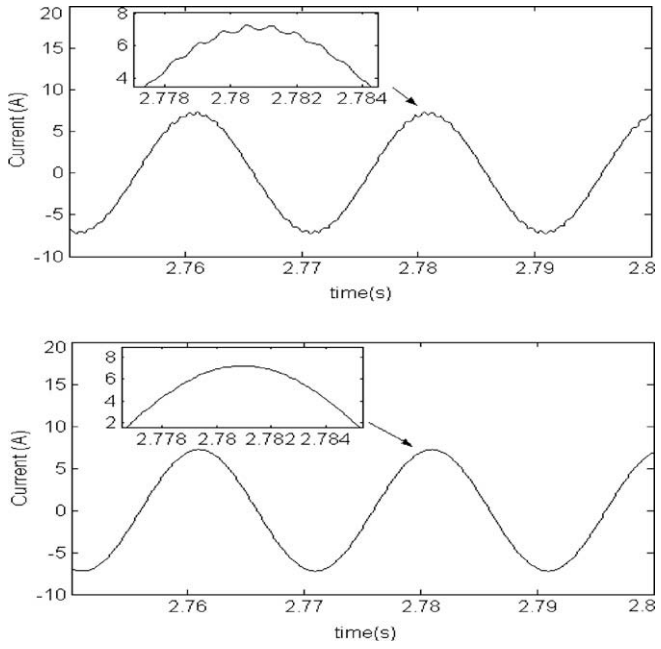

Fig. 18. Stator current wave form at steady-state. Without rotor skew (top) and with rotor skew (bottom). Motor in healthy state.

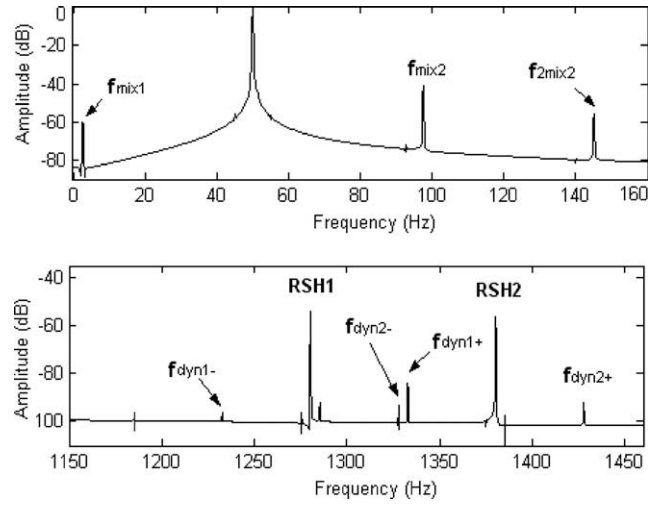

Fig. 19. Simulated stator current spectra in case of mixed radial eccentricity of $\delta_s = 20\%$ and $\delta_d = 20\%$, stator winding YN-connected. Low frequencies (top), high frequencies (bottom).

reason for which the lower RSH associated to a triplen pole pair appears clearly with the upper one even under balanced power supply (Fig. 19).

As predicted, when we consider the Y-connection, only the highest RSH associated to non-triplen pole pair can be seen, while the two RSHs are generated when considering 5% of supply unbalance (Fig. 20). Due to the skew effect, the dynamic eccentricity harmonics are very weak.

5.2.3. Axial eccentricity

Fig. 21 depicts the rotational speed and electromagnetic torque from startup to steady state of the studied IM operating in mixed axial eccentricity conditions compared with the case of mixed radial eccentricity. Load is applied after 0.7 s. The considered axial eccentricity has a static radial eccentricity component of 20% and

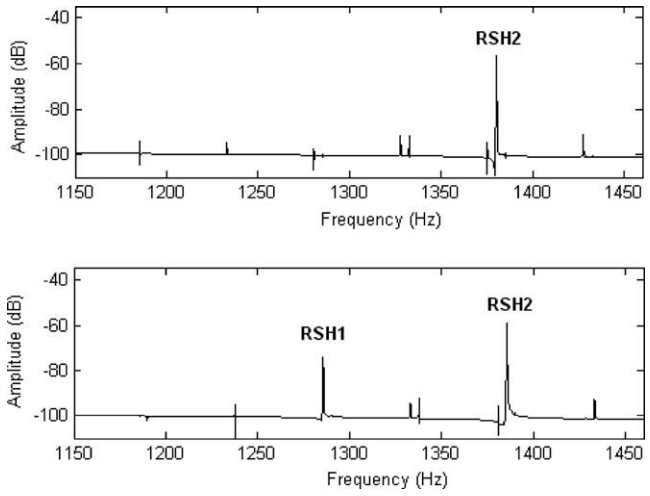

Fig. 20. High rang frequency of simulated stator current spectra in case of mixed radial eccentricity $\delta_s = 20\%$ and $\delta_d = 20\%$, stator winding Y-connected. Balanced supply (top), 5% of supply unbalance (bottom).

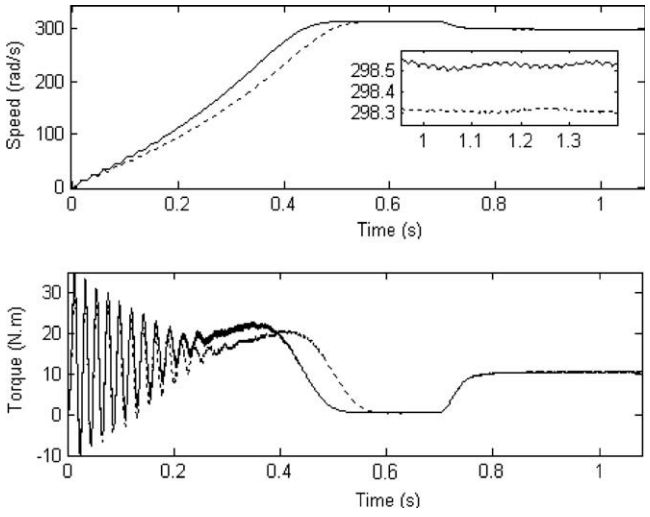

Fig. 21. Speed (top) and electromagnetic torque (bottom) in mixed eccentricity conditions of $\delta_s = 20\%$ and $\delta_{d0} = 20\%$. Pure radial eccentricity (solid line), axial eccentricity with $L_{dy} = l$ (dot line).

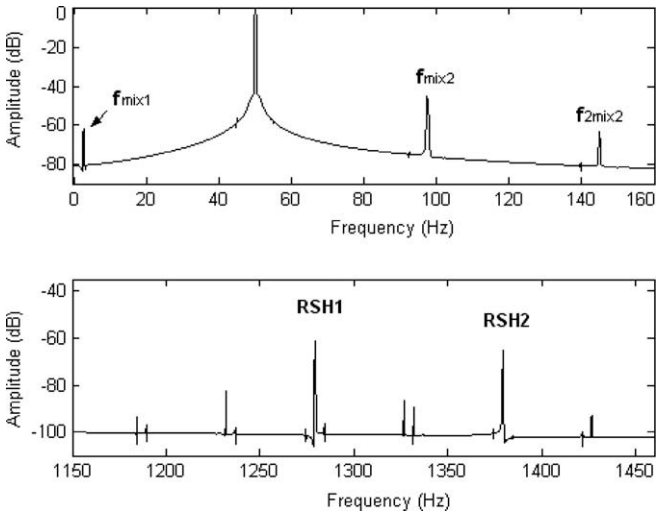

Fig. 22. Simulated stator current spectra in case of mixed axial eccentricity of $\delta_s = 20\%$ radial and $\delta_{d0} = 20\%$ axial with $L_{dy} = l$, stator winding YN-connected. Low frequencies (top), high frequencies (bottom).

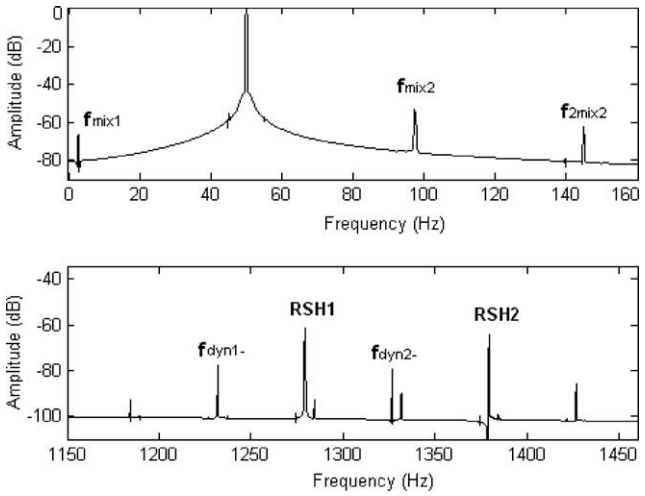

Fig. 23. Simulated stator current spectra in case of mixed axial eccentricity of $\delta_s = 20\%$ radial and $\delta_{d0} = 20\%$ axial with $L_{dy} = l/2$. Stator winding YN-connected. Low frequencies (top), high frequencies (bottom).

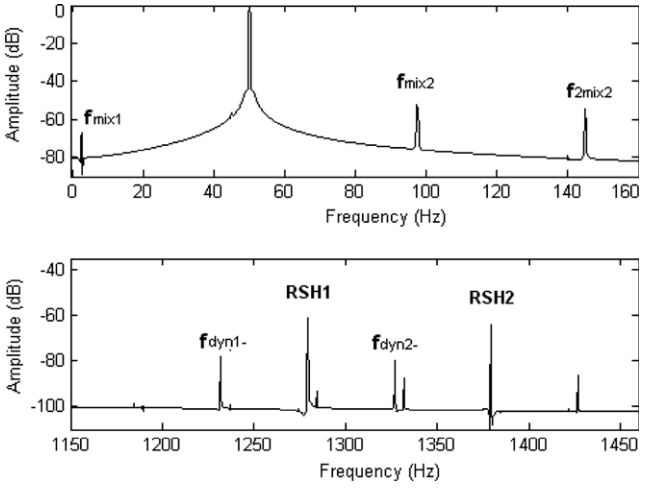

Fig. 24. Simulated stator current spectra in case of mixed axial eccentricity of $\delta_{s0} = 20\%$ axial with $L_{st} = l/2$, and $\delta_d = 20\%$ radial. Stator winding YN-connected. Low frequencies (top), high frequencies (bottom).

dynamic axial eccentricity of $\delta_{d0} = 20\%$ with $L_{dy} = l$. One can note from Fig. 21 that the axial nonuniformity modifies the transient startup as well as the slip in steady state.

The corresponding line current spectra are shown in Fig 22. As is clear, the amplitude of the characteristic components of Eq. (2)

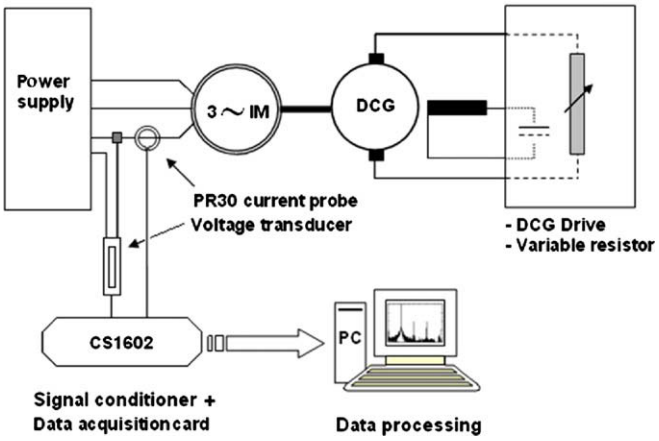

Fig. 25. The experimental setup.

under the same load condition and the same level of eccentricity backside the machine as in pure radial eccentricity (Fig. 19) decrease.

This observation corroborates the observations made from the inductance profiles in Figs. 14 and 15. In case of average zero dynamic eccentricity $\delta_{dy} = 20\%$ with ($L_{dy} = l/2$) and $\delta_s = 20\%$, and average zero static eccentricity $\delta_{st} = 20\%$ with ($L_{st} = l/2$) and and $\delta_d = 20\%$, the amplitudes of the fault-related harmonics is lesser (Figs. 23 and 24). The fault-related current harmonics for radial and axial eccentricity cases are listed in Table 1. In particular, the following have been proved conclusively:

- It is felt that axial eccentricity with low average value ($L_{dy} < l$ or $L_{st} < l$) but high value backside of the rotor can be confused with a radial eccentricity having a small fault level.
- Even though the average eccentricity may be small, with a larger end eccentricity, a rub is still possible at the two ends of the machine. Thus, the axial eccentricity (static, dynamic and mixed eccentricity) can also prove equally catastrophic for the machine as radial eccentricity [15].

6. Experimental verifications

The experimental tests were carried out with the same IM used in simulation (Fig. 25). Separately excited DC generator feeding a variable resistor provides a mechanical load. The voltages and the line current measurements are taken for the motor operating at 50%, 75%, and 100% of the full load. For these two variables, the sampling frequency is 10 kHz. As in simulation, the spectrum

Table 1
Simulation results of radial and axial eccentricity.

Harmonic frequencies for 75% of the full load	Radial eccentricity $\delta_s = 20\%$, $\delta_d = 20\%$		Axial eccentricity ($\delta_s = 20\%$, $\delta_{d0} = 20\%$)			
			$L_{dy} = l$		$L_{dy} = l/2$	
	F (Hz)	A (dB)	F (Hz)	A (dB)	F (Hz)	A (dB)
$f_{mix1} = (f_s - f_r)$	2.6	−60.18	2.6	−61.95	2.46	−61.48
$f_{mix2} = (f_s + f_r)$	97.5	−41.32	97.4	−45.3	97.26	−52.33
$f_{2mix2} = (f_s + 2.f_r)$	145.05	−55.55	145	−63.23	144.93	−59.5
$f_{dyn1-} = [(N_b - 1).(1 - s) - 1] \cdot f_s$	1232.77	−94.4	1231.8	−82.64	1231.5	−77.67
$f_{RSH1} = [N_b \cdot (1 - s) - 1] \cdot f_s$	1280.32	−54.7	1279.4	−61.39	1279.18	−60.15
$f_{dyn1+} = [(N_b - 1).(1 - s) + 1] \cdot f_s$	1332.86	−83.52	1331.8	−89.24	1331.5	−86.16
$f_{dyn2-} = [(N_b + 1).(1 - s) - 1] \cdot f_s$	1327.87	−92.6	1326.8	−86.8	1326.8	−77.6
$f_{RSH2} = [N_b \cdot (1 - s) + 1] \cdot f_s$	1380.3	−58.6	1379.4	−65.19	1379.17	−63.15
$f_{dyn2+} = [(N_b + 1).(1 - s) + 1] \cdot f_s$	1427.9	−91.86	1426.8	−93.07	1426.8	−83.89

Please cite this article in press as: Ghoggal A et al. An improved model of induction motors for diagnosis purposes – Slot skewing ... Energy Convers Manage (2009), doi:10.1016/j.enconman.2009.01.003

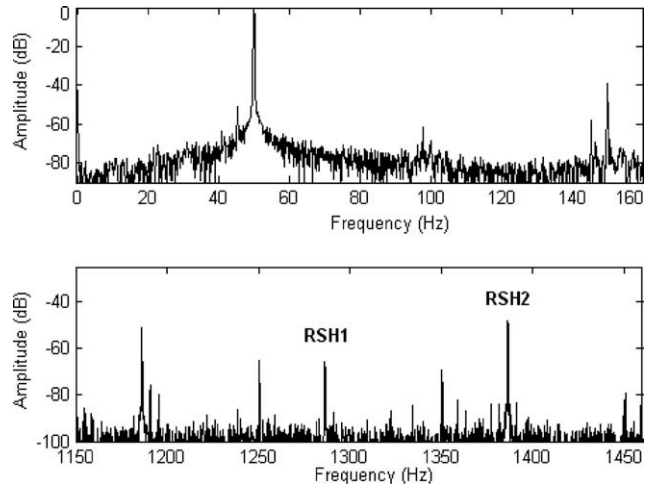

Fig. 26. Stator current spectra in healthy stat. Low frequency (top), high frequency (bottom). 75% of the full load.

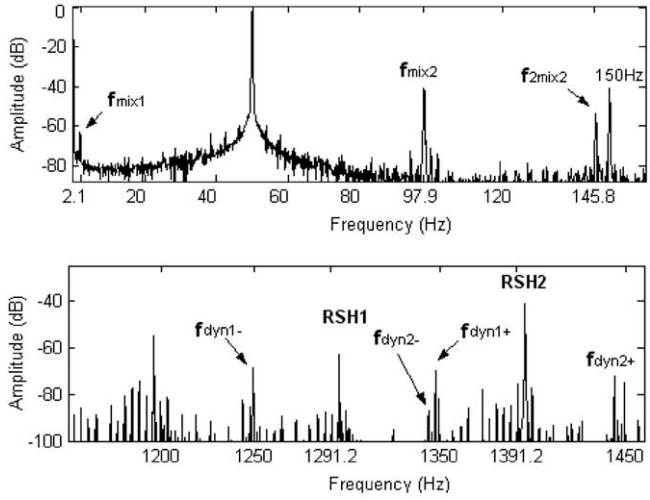

Fig. 27. Stator current spectra with faulty bearings. Low frequency (top), high frequency (bottom). 75% of the full load.

is drawn in the logarithmic magnitude scale and normalized format [22]. The stator winding is Y-connected.

The spectra of Fig. 26 show that even in a healthy state, there are always frequency components but of low amplitudes, this is due to the inherent level of eccentricity, to some degree of rotor asymmetry and from noise introduced by the power supply.

As it has been shown in [30], the contamination in bearings can result in an increase in the magnitude of the components at the eccentricity frequencies predicted by Eq. (2). The present test verifies this result from a real case. For that, a small level of eccentricity was created by replacing the rotor bearings by a set of faulty bearings. Fig. 27 shows that the replacement of the bearings did introduce a small amount of eccentricity. A significant increase of the amplitude of the characteristic frequency components can be easily noticed on both low and high frequency spectra. Lower and upper sideband harmonics close to the fundamental show an increase of approximately 20 dB from the healthy to the faulty case. Furthermore, RSHs and surrounding frequencies also showed up at the exact frequencies predicted by (1). Note that, due to the power supply imbalance, the two RSHs can be seen clearly in the spectra.

Table 2 gathers the frequencies and amplitudes of the fault-related current harmonics with different load conditions. As in simulation, the measured frequencies correlate well with the theoretical prediction. Only some disagreements imputed to the limitation margin of the FFT and the signal transducers can be noted. From Table 2, it can be seen that load affects clearly the magnitudes of the harmonics given by (1) and (2).

For including effectively the harmonics of the power supply, we have injected the acquired voltage data into the simulation tool. In order to corroborate the real faulty case examined, the eccentricity level was approximately chosen after a series of simulation tests covering different fault levels. The upper eccentricity frequency f_{mix2} was taken as a reference. The fault conditions were 20% of static and 20% dynamic radial eccentricity with 10 N m of load torque. The resulting current wave form (Fig. 28) and spectra (Fig. 29) are in good agreement with the actual practical situation (Fig. 27).

Note that this is only an experimental verification reported from a real defect. The main goal was the inspection of the fault-related frequencies in case of faulty bearings. In order to study the evolution laws of the associated magnitudes, an appropriate experimental setup is required.

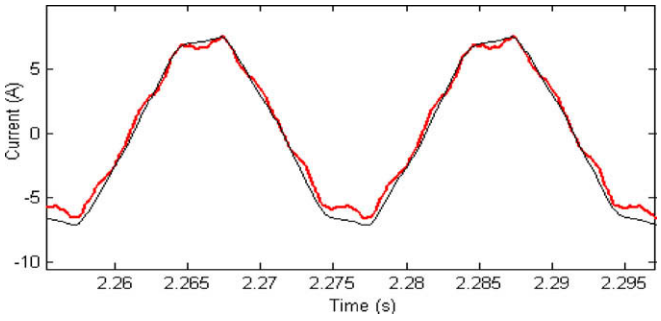

Fig. 28. Stator current wave form at steady state using a real voltage supply: Simulated (thin-black line) and experimental (thick-red line) (For interpretation of color in Fig. 28, readers is referred to the web version of this article).

Table 2
Experimental results for the case of faulty bearings.

Load	50% (s = 0.0214)		75% (s = 0.042)		100% (s = 0.0597)	
	F (Hz)	A (dB)	F (Hz)	A (dB)	F (Hz)	A (dB)
f_{mix1}	1.068	−57.58	2.1	−63.61	3.05	−68.89
f_{mix2}	98.88	−30.46	98	−40.86	97.04	−49.75
f_{2mix2}	147.81	−65.46	145.8	−53.99	144.04	−60.31
f_{dyn1-}	1269	−74.5	1243.3	−69.02	1222.4	−70.5
f_{RSH1}	1320.04	−62.62	1291.2	−60.96	1266.3	−62.5
f_{dyn1+}	1371	−63.84	1343.3	−87.35	1319.4	−76
f_{dyn2-}	1368.8	−84.9	1339.1	−69.5	1313.4	−93.2
f_{RSH2}	1420	−41.85	1391.2	−39.79	1366.4	−40.5
f_{dyn2+}	1468.8	−67.87	1439.1	−71.87	1413.5	−77.39

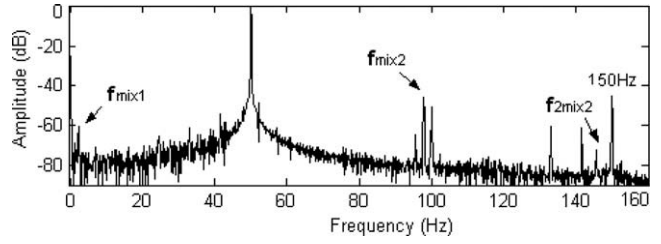

Fig. 29. Simulated stator current spectra in case of mixed radial eccentricity of δ_s = 20% and δ_d = 20%, stator winding YN-connected. Real voltage supply.

7. Conclusion

The multiple coupled circuit model of squirrel cage IM, under the conditions that the motor is healthy/faulty is developed successfully thanks to an extended form of the MWFA. The method enabled the calculation of IM inductances taking into account, first, the harmonics due to the non-sinusoidal distribution of the MMF in the air–gap and, secondly, the effects of rotor bar skewing and the resultant linear rise of MMF across the slots. The resolution of the integrals leading to the machine inductances was greatly simplified by adopting a plane representation of the IM. The new model proves very useful to study the most documented faults operating conditions like radial and axial eccentricity and broken rotor bars and end-rings [29]. Furthermore, it can be extended to study the winding turn-to-turn faults [31]. Based on that, the transient numerical simulation and relevant experiment in IM has been accomplished for the healthy and faulty cases. The proposed method does not require a huge computational capacity and may lead to the development of new tools to precisely diagnose some types of motor defects or faults.

Appendix A

A.1. Machine parameters

$g_0 = 0.000172$ m, $N_b = 28$, $N_e = 36$, $r = 0.0516$ m, $w = 80$, $l = 0.125$ m, $L_b = 0.000172$ H, $L_e = 0.009594$ H, $R_s = 2.86\Omega$, $R_b = 2.856e{-}5\Omega$, $R_e = 1.8560e{-}5\Omega$, $J_r = 0.023976$ kg/m^2, $\gamma = \pi/14 rad$. $\beta = \pi/36$. $f_v = 0.0040$ N m s/rad.

References

[1] Eltabach M, Antoni J, Najjar M. Quantitative analysis of noninvasive diagnostic procedures for induction motor drives. Mech Syst Signal Process 2007;21:2838–56.
[2] Bayindir R, Sefa I. Novel approach based on microcontroller to online protection of induction motors. Energy Convers Manage 2006;48:850–6.
[3] Çalış H, Çakır A. Experimental study for sensorless broken bar detection in induction motors. Energy Convers Manage 2007;49(4):854–62.
[4] Henao H, Razik H, Capolino GA. Analytical approach of the stator current frequency harmonics computation for detection of induction machine rotor faults. IEEE Trans Ind Appl 2005;41(3):24–34.
[5] Antonio-Daviu J, Jover P, Riera M, Arkkio A, Roger-Folch J. DWT analysis of numerical and experimental data for the diagnosis of dynamic eccentricities in induction motors. Mech Syst Signal Process 2007;21(6):2575–89.
[6] Toliyat HA, Lipo TA. Transient analyse of induction machines under stator, rotor bar and end ring faults. IEEE Trans Energy Convers 1995;10(2):241–7.
[7] Toliyat HA, Arfeen MS, Parlos AJ. A methode for dynamic simulation of air–gap eccentricity in induction machine. IEEE Trans Ind Appl 1996;32(4):910–8.
[8] Al-Nuaim NA, Toliyat HA. A novel method for modelling dynamic air–gap eccentricity in synchronous machines based on modified winding function theory. IEEE Trans Energy Convers 1998;13(2):156–62.
[9] Nandi S. Modeling of induction machines including stator and rotor slot effects. IEEE Trans Ind Appl 2004;40(4):1058–65.
[10] Nandi S. A detailed model of induction machines with saturation extendable for fault analysis. IEEE Trans Ind Appl 2004;40:1302–9.
[11] Jung JH, Lee JJ, Kwon BH. Online diagnosis of induction motors using MCSA. IEEE Trans Ind Electron 2006;53(6):1842–52.
[12] Acosta GG, Verucchi CJ, Gelso ER. A current monitoring system for diagnosing electrical failures in induction motors. Mech Syst Signal Process 2004;20:953–65.
[13] Cameron JC, Thomson WT, Dow AB. Vibration and current monitoring for detecting air–gap eccentricity in large induction motors. IEE 1986;133(3):155–63.
[14] Nandi S, Bharadwaj RM, Toliyat HA. Performance analyse of three-phase induction motor under mixed eccentricity condition. IEEE Trans Energy Converse 2002;17(3):392–9.
[15] Li X, Wu Q, Nandi S. Performance analysis of three-phase induction machine with inclined static eccentricity. IEEE Trans Ind Appl 2007;43(2):531–41.
[16] Faiz J, Ardekanei IT. Extension of winding function theory for nonuniform air–gap in electric machinery. IEEE Trans Magn 2002;38(6):3654–7.
[17] Joksimovic MG, Durovic DM, Obradovic AB. Skew and linear rise of MMF across slot modelling–Winding function approach. IEEE Trans Energy Converse 1999;14(3):315–20.
[18] Tenhunen A, Benedetti T, Holopainen T.P, Arkkio A. Electromagnetic forces in cage induction motors with rotor eccentricity. In: Proceeding of IEMDC ;1–4 June, vol. 3; 2003. p. 1616–22.
[19] Kelk HM, Eghbali A, Toliyat HA. Modeling and analysis of cage induction motors under rotor misalignment and air gap eccentricity. In: Proceeding of IEEE IAS, 2–6 October, vol. 2; 2005. p. 1324–28.
[20] Cabanas MF, Melero MG, Aleixandre JG, Solares J. Shaft misalignment diagnosis of induction motors using spectral analysis: a theoretical approach. In: Proceeding of ICEM Vigo, Spain; 1996.
[21] Bossio G, Angelo CD, Solsona J, García G, Valla MI. A 2-D Model of the induction machine: extension of the modified winding function approach. IEEE Trans Energy Convers 2004;19(1):144–50.
[22] Ghoggal A, Aboubou A, Zouzou SE, Sahraoui M, Razik H. Considerations about the modeling and simulation of air–gap eccentricity in induction motors. In: Proceeding of IEEE IECON, 06–10 November; 2006.
[23] Bossio G, Angelo CD, Solsona J, García GO, Valla MI. Application of an additional excitation in inverter-fed induction motors for air–gap eccentricity diagnosis. IEEE Trans Energy Converse 2006;21(4):839–47.
[24] Nandi S, Ahmed S, Toliyat HA. Detection of rotor slot and other eccentricity related harmonics in a three-phase induction motor with different rotor cages. IEEE Trans Energy Converse 2001;16(3):253–60.
[25] Ghoggal A, Sahraoui M, Aboubou A, Zouzou SE, Razik H. An improved model of the induction machine dedicated to faults-detection – extension of the modified winding function. In: Proceeding of IEEE ICIT 2005, Hong-Kong, China, 14–17, December; 2005.
[26] Sobol IM. On quasi-Monte Carlo integrations. Math Comput Simulation 1998;47:103–12.
[27] Harvey G, Tobochnik J, Wolfgang C. Numerical integration and Monte Carlo methods; 2001.[chapter 11]
[28] Heming L, Liling S, Boqiang X. Research on transient behaviors and detection methods of stator winding inter-turn short circuit fault in induction motors based on multi-loop mathematical model. In: Proceeding of IEEE ICEMS, 27–29 September; 2005, vol. 3. p. 1951–1955.
[29] Zouzou SE, Ghoggal A, Aboubou A, Sahraoui M, Razik H. Modelling of induction machines with skewed rotor slots dedicated to rotor faults. In: Proceeding of IEEE Sdemped 2005, Vienna, Austria; 2005.
[30] Knight AM, Bertani SP. Mechanical fault detection in a medium-sized induction motor using stator current monitoring. IEEE Trans Energy Convers 2005;20:753–60.
[31] Sahraoui M, Ghoggal A, Zouzou SE, Aboubou A, Razik H. Modelling and detection of inter-turn short circuits in stator windings of induction motor. In: Proceeding of IEEE. IECON 2006, Paris-France; 2006.

Please cite this article in press as: Ghoggal A et al. An improved model of induction motors for diagnosis purposes – Slot skewing ... Energy Convers Manage (2009), doi:10.1016/j.enconman.2009.01.003